Impact of Wall-Slip on Real Shear Thickening Fluid Flow Behavior in Rectangular Channels: Insights from LBM and Theoretical Modeling

Garima Vishal, **Ashish Garg**, **Jayati Sarkar***, **Sudip K. Pattanayek***

Department of Chemical Engineering, Indian Institute of Technology Delhi, India

March 1, 2024

Abstract

The liquid slip phenomenon are pivotal for understanding fluid behavior at small scales and has been investigated using the lattice Boltzmann method (LBM). Boundary conditions for the lattice Boltzmann liquid flow simulation, however, are much beyond from ideal and how to precisely determine the boundary conditions for liquid flow with slip remains a challenge. In this study, we integrate the slip boundary condition for fluid flow for Newtonian as well as non-Newtonian fluid. Our primary emphasis is to comprehend the influence of slip effects on the flow characteristics of real shear-thickening fluid (STF), encompassing Newtonian, shear-thinning, and shear-thickening behaviors under varying applied stresses or strain rates. In order to achieve this, we have introduced the combination of modified bounce back and specular reflection (MBSR) scheme and half way bounce back and specular reflection (HBSR) scheme. In theory, the interactions between the parameters of the combination and the slip length are explicitly deduced. The specified combination parameter is decided by the slip length given and the relaxation time. These slip boundary conditions are analyzed for their distinct results. Our process has been tested for accuracy and reliability for Newtonian flow as well as non-Newtonian flow and the results are compared with the analytical solution. We also develop a theoretical model to elucidate the flow characteristics of real shear-thickening fluid (STF) in a channel with slip effects. Investigating pressure and channel height variations, we observe nuanced responses. Initially, under increasing pressure, the regime with Newtonian flow rate $Q1$ dominates, reaching a peak. As pressure rises yielding dominance to another regime with shear-thinning flow rate $Q2$, while regime with shear-thickening flow rate $Q3$ remains zero. Further pressure escalation prompts a monotonically increasing trend in $Q3$, achieving dominance. Simultaneously, $Q1$ and $Q2$ approach zero. These trends hold true with and without slip effects, with higher flow rates in the presence of slips for a given pressure drop and viscosity. Additionally, as channel height increases, $Q1$ predominates at lower heights, transitioning to dominance by $Q2$ and then $Q3$ at larger heights.

Keywords: Lattice Boltzmann Method, Shear thickening Fluid, STF theoretical model, mimicking real STF viscosity model, combine of Newtonian, shear thinning and shear thickening viscosity, wall-slip.

***Email**: **sudip@chemical.iitd.ac.in, jayati@chemical.iitd.ac.in**

1

1 Introduction

In recent years, researchers have shown a growing interest in understanding the phenomenon of liquid slip [1–4], where a fluid flows near a solid surface with a relative motion between the two, resulting in a slip velocity [3, 5] at the boundary. Slip conditions, deviating from the conventional no-slip assumption in fluid mechanics, gain prominence in microfluidics and nanofluidics where viscosity effects become substantia [6, 7]. Notably, slip reduces drag in nanoflows, optimizing efficiency in nanoscale devices, and finds applications in industrial lubrication. To effectively use numerical simulations, it's crucial to establish appropriate slip boundary conditions. These boundary conditions play a vital role in accurately modeling and understanding slip effects, making them a significant aspect of research in this field.

The slip length is determined by the characteristics of the fluid-solid system, including viscosity, surface roughness, and ambient conditions. Viscosity influences the ease of fluid slip, while surface roughness and ambient conditions contribute to the deviation from the traditional no-slip behavior at the fluid-solid interface [8]. We have a range of the slip length considered in literature which depends on the height of the domain. To investigate and simulate liquid slip, computational methods have become essential tools, and the lattice Boltzmann technique [9–12] is one such method widely used for its versatility and ability to handle complex fluid behaviors. However, when simulating fluid flow with slip using the lattice Boltzmann method (LBM), determining accurate boundary conditions becomes a challenging task. The researchers have been actively working on improving the accuracy of slip boundary conditions in lattice Boltzmann simulations. Within the realm of LBM, significant research has been dedicated to addressing slip boundary conditions.

In LBM, there exist two primary approaches for implementing slip boundary conditions. The first strategy involves directly constructing the slip velocity using Navier's slip model. Subsequently, velocity boundary conditions are employed to simulate the slip velocity. Tian et al., for instance, employed a second-order implicit scheme to calculate the first-order derivative of the slip velocity at the boundary [13]. Meanwhile, Zheng et al. introduced a coupling between the momentum equation, energy equation, and LBM to obtain the slip velocity, effectively circumventing the challenge of computing the second-order derivative of the slip velocity [14]. Both Tian et al. and Zheng et al. applied the non-equilibrium extrapolation scheme to achieve slip boundary conditions, but they did not explicitly consider the numerical slip velocity generated by the velocity boundary conditions.The lattice Boltzmann method has proven to be a versatile and robust tool for studying microchannel flows with slip boundary conditions, and researchers have explored various strategies to accurately implement these conditions within the framework of LBM. These efforts contribute to a deeper understanding of fluid behavior in microchannels, particularly when slip effects come into play.

Slip issues are indeed expected in shear-thickening fluids (STFs) due to the nature of their rheological behavior. STFs exhibit a significant increase in viscosity at high shear rates, which can lead to the formation of a percolated network of particles that prevents the fluid from flowing smoothly and also start behaving like a soft solid [15]. This phenomenon, known as discontinuous shear thickening (DST), can result in a stick–slip behavior between the fluid acting like a soft solid and the wall, where the

2

fluid experiences periods of high stress and low shear rate, followed by sudden jumps in stress and shear rate near wall [16]. Slip affects the flow of shear-thickening fluids (STFs) by altering the boundary conditions and the resulting stress distribution. When slip occurs, the fluid's viscosity increases to such an extent that it prevents the fluid from flowing smoothly at the boundaries, leading to stick–slip behavior [17]. Further, wall slip can result in non-uniform flow profiles across the fluid thickness, leading to flow heterogeneity and variations in the observed rheological behavior [18]. This can complicate the analysis of shear-thickening mechanisms and limit the applicability of models for describing the fluid's flow behavior. In practical applications of shear-thickening fluids, such as in industrial processes or consumer products, wall slip can affect the performance and stability of the material. For example, in applications involving coating or lubrication, excessive wall slip may lead to uneven or inconsistent coverage, impacting product quality and performance [19].

In this study, we have proposed a novel approach to incorporate slip boundary conditions for both Newtonian and non-Newtonian fluids. To implement slip boundary conditions effectively, the authors introduce a combination of two schemes: the modified bounce-back and specular reflection (MBSR) scheme and the half-way bounce-back and specular reflection (HBSR) scheme [3]. These schemes are used to define how fluid particles interact with the solid boundary in the lattice Boltzmann simulation. The key innovation lies in how the combination of these schemes is chosen. The study explicitly derives relationships between the combination parameters and the slip length. The slip length is a critical parameter that characterizes the extent of slip at the solid-fluid interface. By understanding how to adjust the combination parameters based on the desired slip length and the relaxation time (a parameter in the lattice Boltzmann method that controls the rate of convergence to equilibrium), researchers can tailor the simulation to accurately represent different slip conditions. The research then systematically analyzes the proposed slip boundary conditions and assesses their impact on simulation outcomes. This analysis helps uncover the distinct results that arise from these boundary conditions, shedding light on how slip affects fluid behavior in various scenarios. To validate the proposed method, the researchers rigorously test its accuracy and reliability. They conduct simulations for both Newtonian and non-Newtonian flows and compare their results with analytical solutions. This comparison serves as a benchmark for evaluating the performance of the new slip boundary conditions.

We consider a shallow rectangular channel characterized by dimensions: length L, width W, and height H, satisfying the conditions $H \ll W$ and $H \ll L$, as depicted in Figure 1. A pressure difference prompts a flow rate Q_{total} in the x_1 direction. At $x_1 = 0$, a pressure field $p(x_1)$ is introduced at the reservoir, while the exit pressure is $p(x_1 = L)$ as illustrated in Figure 1. The theoretical model without slips was already derived in our previous study [20]. Here, in this derivation, we also incorporate the effect of slips λ to understand flow characteristics under slips for the real STF flows.
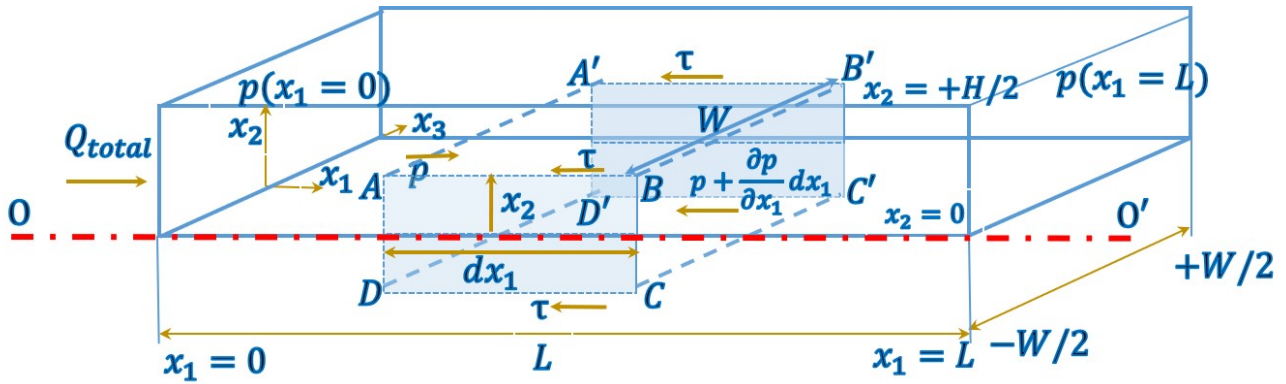
3

Figure 1: Schematic diagram of the upper half part (above the red color dashed line OO') of the shallow channel of length L, cross–sectional width W, and height H. The Cartesian axis is taken at the mid plane of the channel.

2 Numerical method

The Lattice Boltzmann Method (LBM) operates on a lattice grid and models the behavior of fluid particles as they move and collide in discrete time steps. The LBM simulations has following initialization, collision and streaming steps. These steps are same to that previously used for analysis of various systems[20, 21]. The boundary conditions are to be different to incorporate the deviation from "no-slip" condition.

2.1 Boundary conditions

Here we are considering the slip boundary conditions which corresponds to nonzero velocity at the wall. In the context of the Lattice Boltzmann Method (LBM) slip boundary condition can be understood through the "half-way bounce-back condition"[3] and "half-way specular bounce-back condition" methods[3], which are particularly used for modeling fluid flow with slip boundary. In the half-way bounce-back condition, fluid particles encountering a solid boundary rebound directly back in the opposite direction, effectively reflecting off the boundary. This is implemented by setting the distribution functions of fluid particles moving towards the solid boundary equal to those of particles moving away from the boundary, but in the opposite direction as shown in 2 (a) . The half-way specular bounce-back condition extends this concept by incorporating specular reflection, where the angle of incidence not equals the angle of reflection. Here, fluid particles not only bounce back upon encountering the solid boundary but also undergo specular deflection from the 180 degree reflection, simulating the behavior of particles bouncing off a smooth, solid surface. In both methods, modifications to the distribution functions of fluid particles at boundary nodes are made to accurately simulate the desired boundary behavior, thereby allowing for accurate modeling of fluid flow phenomena near boundaries for slip in LBM simulations. The bounce back boundary condition has been explained in figure 2 (a) where the

4

density distribution function reflects back from the wall in the given direction of the particle distribution functions f_0, f_1, f_3, f_4, f_7 and f_8 through the streaming step, while the distributions f_2, f_5 and f_6 remain unknown. However, in the combined half-way bounce-back condition and half-way specular bounce-back condition method (referred to as the half-way method) the unkowns remains same as bounce back boundary condition but the direction of reflection changes according to the accomodation coefficient (r) depiction is given in 2 (b). Accomodation coefficient is the extend of deflection from the 180^0 which depends on slip length and slip velocity.
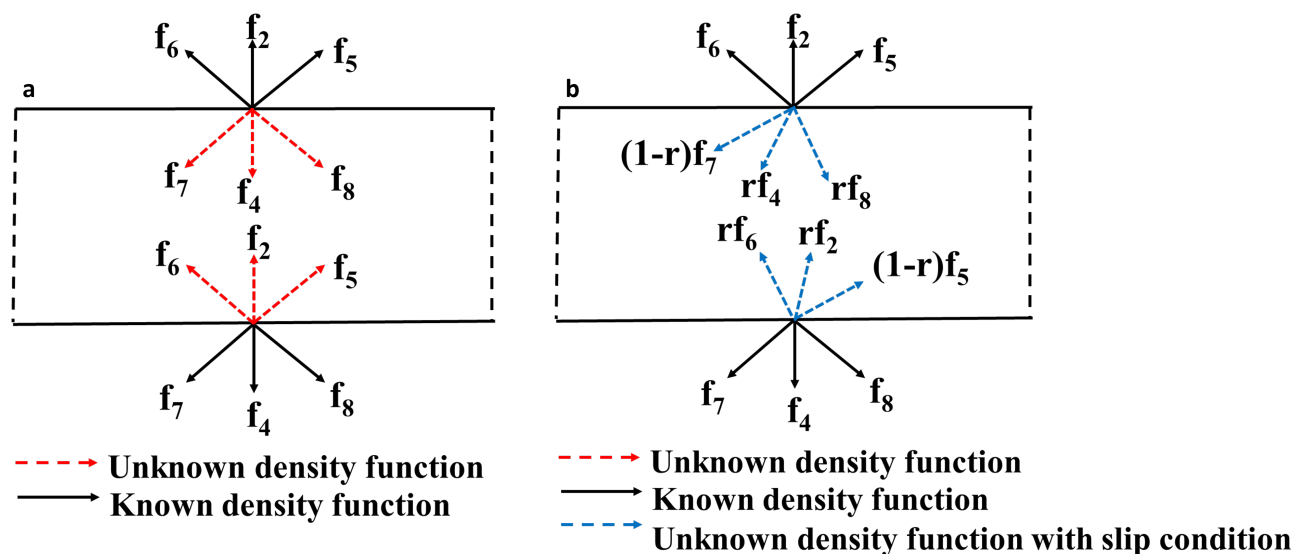

Figure 2: The distribution functions for (a) bounce back boundary condition (b) specular bounce back boundary condition

The expressions for the unknown particle distribution functions are provided below.
For the bottom wall

$$f_2\left(x_1, x_{2_0}, t + \Delta t\right) = f_4^*\left(x_1, x_{2_0}, t\right) \tag{1}$$

$$f_5\left(x_1, x_{2_0}, t + \Delta t\right) = r f_7^*\left(x_1, x_{2_0}, t\right) + (1 - r) f_8^*\left(x_1, x_{2_0}, t\right) \tag{2}$$

$$f_6\left(x_1, x_{2_0}, t + \Delta t\right) = r f_8^*\left(x_1, x_{2_0}, t\right) + (1 - r) f_7^*\left(x_1, x_{2_0}, t\right) \tag{3}$$

For the top wall

$$f_4\left(x_1, x_{2_{N-1}}, t + \Delta t\right) = f_2^*\left(x_1, x_{2_N}, t\right) \tag{4}$$

$$f_7\left(x_1, x_{2_{N-1}}, t + \Delta t\right) = r f_5^*\left(x_1, x_{2_N}, t\right) + (1 - r) f_6^*\left(x_1, x_{2_N}, t\right) \tag{5}$$

$$f_8\left(x_1, x_{2_{N-1}}, t + \Delta t\right) = r f_6^*\left(x_1, x_{2_N}, t\right) + (1 - r) f_5^*\left(x_1, x_{2_N}, t\right), \tag{6}$$

where $f_2^*\left(x_1, x_{2_N}, t\right)$, $f_4^*\left(x_1, x_{2_0}, t\right)$, $f_5^*\left(x_1, x_{2_N}, t\right)$, $f_6^*\left(x_1, x_{2_N}, t\right)$, $f_7^*\left(x_1, x_{2_0}, t\right)$, and $f_8^*\left(x_1, x_{2_0}, t\right)$, are the distribution function after the collision.

5

Calculating the accommodation coefficient is the most difficult part of solving the preceding equations. We must determine the link between the slip length and the accommodation coefficient for liquid flow.

It is important to choose the appropriate boundary condition based on the physics of the problem you are simulating. The choice of boundary condition can significantly impact simulation accuracy and results. Proper implementation of boundary conditions ensures that the simulated fluid behaves realistically near domain boundaries and interacts correctly with solid surfaces or other boundary features.

3 Theoretical Model with slips for mimicking real STF viscosity

3.1 Governing equations (Cauchy equations)

The Cauchy's equation [22] and the continuity equation for an incompressible fluid are given by

$$\rho\left(\frac{\partial \boldsymbol{v}}{\partial t} + (\boldsymbol{v} \cdot \boldsymbol{\nabla})\boldsymbol{v}\right) = -\boldsymbol{\nabla}p - \rho\boldsymbol{g} + \boldsymbol{\nabla}.\boldsymbol{\tau},$$
$$\boldsymbol{\nabla} \cdot \boldsymbol{v} = 0,$$
(7a,b)

where $\boldsymbol{v} = [u, v, w]$ is the fluid velocity, p is the fluid pressure, ρ is the fluid density, $\boldsymbol{g}$ is the gravitational body force along negative x_2 direction, and $\boldsymbol{\tau}$ is the total deviatoric stress tensor.

3.2 Boundary conditions

We assume that the fluid cannot penetrate the channel wall. Therefore, on the boundary Γ.

$$\boldsymbol{v} \cdot \boldsymbol{n}_{\text{wall}} = 0,$$
(8)

where $\boldsymbol{n}_{\text{wall}}$ is the unit outward normal vector on the wall. We assume the slip boundary condition at wall [23, 24], which says

$$(1 - \Theta)(\boldsymbol{m}_{\text{wall}}^T \cdot \mathcal{D}(\boldsymbol{v})) \cdot \boldsymbol{n}_{\text{wall}} + \Theta\boldsymbol{v} \cdot \boldsymbol{m}_{\text{wall}} = 0,$$
(9)

where $\boldsymbol{m}_{\text{wall}}$ is the tangential unit vector along the channel wall and $\mathcal{D}(\boldsymbol{v}) = (\boldsymbol{\nabla}\boldsymbol{v} + \boldsymbol{\nabla}\boldsymbol{v}^T)/2$ is the deformation tensor. Also, the arbitrary parameter Θ meets $0 \leq \Theta \leq 1$. Here, $\Theta = 0$ and 1 correspond to pure-slip and no-slip boundary conditions. The symmetry boundary condition at the centreline of the channel $x_2 = 0$ demands the normal velocity to the centreline and the traction tangential to the centreline (or the shear rate) are both zero. These two conditions can be expressed as

$$\boldsymbol{v} \cdot \boldsymbol{n}_{\text{centreline}} = 0,$$
(10)

and

$$\boldsymbol{t} \cdot \boldsymbol{m}_{\text{centreline}} = 0,$$
(11)

respectively, where $\boldsymbol{n}_{\text{centreline}}$ and $\boldsymbol{m}_{\text{centreline}}$ are the unit normal and unit tangent vector to the symmetry boundary, respectively. The traction on the boundary, which is equivalent to a Neumann boundary condition, is expressed as

$$\boldsymbol{t} = \boldsymbol{n}_{\text{centreline}}^T \cdot (-p\boldsymbol{I} + \boldsymbol{\tau}).$$
(12)

6

3.3 Mimicking real STF viscosity model

To model the fluid behavior, we use a real mimicking STF viscosity model, which in one dimension is given by

$$\eta(\dot{\gamma}) = \left\{ \begin{array}{lll} \eta_{\text{I}}(\dot{\gamma}) = m_1 & \text{for} & 0 < \dot{\gamma} \leq \dot{\gamma}_1 \\ \eta_{\text{II}}(\dot{\gamma}) = m_2 \dot{\gamma}^{n_2-1}, n_2 < 1 & \text{for} & \dot{\gamma}_1 < \dot{\gamma} \leq \dot{\gamma}_2 \\ \eta_{\text{III}}(\dot{\gamma}) = m_3 \dot{\gamma}^{n_3-1}, n_3 > 1 & \text{for} & \dot{\gamma}_2 < \dot{\gamma} \end{array} \right\} \tag{13}$$

3.4 2D planar model

We consider fully developed, steady laminar flow of an incompressible mimicking real STF viscosity fluid between two parallel plates under lubrication limits in a rectangular channel of height H and width W. We show the a schematic diagram of the upper half part (above the red color dashed line OO') of the shallow channel in Figure 1. The channel is assumed to be sufficiently long and wide in comparison to the height (that is, $H/W \ll 1$, and $H/L \ll 1$) to use a two–dimensional planar model [15, 22]. The mid–plane between the plates will be taken as the origin with the flow domain extending from $z = -H/2$ to $z = +H/2$.

Further suppose that the Cartesian velocity components u and w along longitudinal and vertical directions x_1 and x_2, respectively. The x_2 coordinate is measured from the channel's mid–plane. Therefore, using the lubrication assumptions in the shallow cross–section of the channel as shown in [25], we retain the leading order terms. Using the impermeable solid–wall boundary condition, we get $w(x_2 = -H/2) = w(x_2 = H/2) = 0$. In the leading order terms, using the impermeable solid-wall boundary condition, the normal velocity vanishes everywhere. Further, we neglect the pressure gradient and velocity components normal to the channel wall. Also, we neglect all body forces. Under these assumptions, for $H/W \ll 1$, and $H/L \ll 1$, we show a fluid element $ABCDD'A'B'C'$ in Figure 1. The force balance on this element can be calculated as the pressure p and $p + \frac{\partial p}{\partial x_1}dx_1$ acting on the $AA'D'D$, and $BB'C'C$ surfaces, respectively along the positive and negative x_1 directions. Also, the shear stress $\tau_{x_1 x_2}$ is acting along the negative x_1 direction on both the surfaces $DD'C'C$ and $AA'B'B$. Dropping the $x_1 x_2$ notation from the stress, the force balance can be written as [26, 27]

$$2Wpx_2 - 2W\left(p + \frac{\partial p}{\partial x_1}\partial x_1\right)x_2 = 2W \, \tau dx_1, \tag{14}$$

which implies

$$\tau = \eta\dot{\gamma} = -\frac{\partial p}{\partial x_1}x_2 \tag{15}$$

where η is mimicking the real STF viscosity. As stress is increasing linearly with x_2, therefore for constant and thinning viscosity, the shear rate will also increase with x_2. Further for moderate thickening of viscosity, the shear rate would also increase with x_2. Therefore, the channel could be divided into three regions from the mid-plane.

7

3.4.1 In region I: $\eta = \eta_I$ for $0 \leq z \leq z_1$

$$\eta_I \dot{\gamma} = m_1 \dot{\gamma} = -\frac{\partial p}{\partial x_1} x_2, \Rightarrow \dot{\gamma} = -\frac{\partial u}{\partial x_2} = \left(-\frac{\partial p}{\partial x_1} \frac{1}{m_1} \right) x_2 \tag{16}$$

Upon integration, we get

$$-u_1 = \frac{1}{2} \left(-\frac{\partial p}{\partial x_1} \frac{1}{m_1} \right) x_2{}^2 + c_1, \tag{17}$$

and the volume flow rate in a channel is given by

$$Q_1 = 2 \, W \int_0^{z_1} u_1 dx_2 \tag{18}$$

Integrating the right–hand–side of the above equation, we get

$$Q_1 = 2 \, W \left| \frac{1}{6} \left(-\frac{\partial p}{\partial x_1} \frac{1}{m_1} \right) z_1^3 + c_1 z_1 \right. \tag{19}$$

where $z_1 = \left(m_1 \, \dot{\gamma}_1 \middle/ -\frac{\partial p}{\partial x} \right)$.

3.4.2 In region II: $\eta = \eta_{II}$ for $z_1 \leq z \leq z_2$

$$\eta_{II} \dot{\gamma} = m_2 \dot{\gamma}^{n_2-1} \dot{\gamma} = m_2 \dot{\gamma}^{n_2} = -\frac{\partial p}{\partial x_1} x_2 \tag{20}$$

$$\dot{\gamma} = -\frac{\partial u}{\partial x_2} = \left(\frac{-\partial p}{\partial x_1} \frac{1}{m_2} \right)^{\frac{1}{n_2}} x_2^{\frac{1}{n_2}} \tag{21}$$

From integrating, we get

$$-u_2 = \frac{(n_2)}{(n_2+1)} \left(\frac{-\partial p}{\partial x_1} \frac{1}{m_2} \right)^{\frac{1}{n_2}} x_2^{\frac{(n_2+1)}{(n_2)}} + c_2 \tag{22}$$

And the volume flow rate in a channel is given by

$$Q_2 = 2 \, W \int_{z_1}^{z_2} u_2 dx_2 \tag{23}$$

Integrating the right–hand–side of the above equation (23) , we get

$$Q_2 = 2 \, W \left(\frac{n_2^2}{(2n_2+1)(n_2+1)} \right) \left(\frac{-\partial p}{\partial x_1} \frac{1}{m_2} \right)^{\frac{1}{n_2}} x_2^{\frac{(n_2+1)}{n_2}} + c_2 x_2 \Big|_{z_1}^{z_2} \tag{24}$$

where $z_2 = \left(m_2 \, \dot{\gamma}_2^{n_2} \middle/ -\frac{\partial p}{\partial x} \right)$.

8

3.4.3 In region III: $\eta = \eta_{III}$ for $z_2 \leq z \leq H/2$

$$\eta_{III}\dot{\gamma} = m_3\dot{\gamma}^{n_3-1}\dot{\gamma} = \dot{\gamma}^{n_3} = \frac{-\partial p}{\partial x_1}x_2 \tag{25}$$

$$\dot{\gamma} = -\frac{\partial u}{\partial x_2} = \left(\frac{-\partial p}{\partial x_1}\frac{1}{m_3}\right)^{\frac{1}{n_3}}x_2^{\frac{1}{n_3}} \tag{26}$$

Upon integration, we get

$$-u_3 = \frac{n_3}{(n_3+1)}\left(\frac{-\partial p}{\partial x}\frac{1}{m_3}\right)^{\frac{1}{n_3}}x_2^{\frac{(n_3+1)}{n_3}} + c_3 \tag{27}$$

And the volume flow rate in a channel is given by

$$Q_3 = 2\,\text{W}\int_{z_2}^{H/2}u_3dx_2 \tag{28}$$

Integrating the right–hand–side of the above equation (28) , we get

$$Q_3 = 2\,\text{W}\left(\frac{n_3^2}{(2n_3+1)(n_3+1)}\right)\left(\frac{-\partial p}{\partial x_1}\frac{1}{m_3}\right)^{\frac{1}{n_3}}x_2^{\frac{(2n_3+1)}{n_3}} + c_3x_2\Bigg|_{z_2}^{H/2} \tag{29}$$

3.4.4 Calculation of c_1, c_2, and c_3

Using the boundary condition that at $x_2 = \text{H}/2$, $u_3 = \lambda\left|\dfrac{\partial u_3}{\partial x_2}\right|$ (due to slip condition), where λ is the slip length defined as $\lambda = \dfrac{(1-\Theta)}{2\Theta}|n_{\text{wall},x_2}| \geq 0$, and n_{wall,x_2} is the x_2 component of unit vector $\boldsymbol{n}_{\text{wall}}$. Therefore from equation (27), we get

$$c_3 = \lambda\left|\left(-\frac{\partial p}{\partial x_1}\frac{1}{m_3}\right)^{1/n_3}\left(\frac{H}{2}\right)^{1/n_3}\right| - \frac{n_3}{(n_3+1)}\left(\frac{-\partial p}{\partial x_1}\frac{1}{m_3}\right)^{\frac{1}{n_3}}(H/2)^{\frac{(n_3+1)}{n_3}} \tag{30}$$

Further, using another boundary condition that at $x_2 = z_2$, $u_3 = u_2$ (due to continuous velocity condition), therefore from equations (22), and (27), we get

$$c_2 = \frac{n_3}{(n_3+1)}\left(\frac{-\partial p}{\partial x}\frac{1}{m_3}\right)^{\frac{1}{n_3}}\left((z_2)^{\frac{(n_3+1)}{n_3}} - (H/2)^{\frac{(n_3+1)}{n_3}}\right) - \frac{n_2}{(n_2+1)}\left(\frac{-\partial p}{\partial x_1}\frac{1}{m_2}\right)^{\frac{1}{n_2}}z_2^{\frac{(n_2+1)}{(n_2)}}$$
$$+\lambda\left|\left(-\frac{\partial p}{\partial x_1}\frac{1}{m_3}\right)^{1/n_3}\left(\frac{H}{2}\right)^{1/n_3}\right| \tag{31}$$

Similarly, using another boundary condition that at $x_2 = z_1$, $u_2 = u_1$ (due to continuous velocity condition), therefore from equations (17), and (22), we get

9

$$c_1 = \frac{(n_2)}{(n_2+1)} \left(\frac{-\partial p}{\partial x_1} \frac{1}{m_2} \right)^{\frac{1}{n_2}} z_1^{\frac{(n_2+1)}{(n_2)}} + \frac{n_3}{(n_3+1)} \left(\frac{-\partial p}{\partial x} \frac{1}{m_3} \right)^{\frac{1}{n_3}} \left((z_2)^{\frac{(n_3+1)}{n_3}} - (H/2)^{\frac{(n_3+1)}{n_3}} \right)$$
$$- \frac{n_2}{(n_2+1)} \left(\frac{-\partial p}{\partial x_1} \frac{1}{m_2} \right)^{\frac{1}{n_2}} z_2^{\frac{(n_2+1)}{(n_2)}} - \frac{1}{2} \left(-\frac{\partial p}{\partial x_1} \frac{1}{m_1} \right) z_1^2 \qquad (32)$$
$$+ \lambda \left| \left(-\frac{\partial p}{\partial x_1} \frac{1}{m_3} \right)^{1/n_3} \left(\frac{H}{2} \right)^{1/n_3} \right|$$

The total flow rate can be written as

$$Q_{\text{total}} = Q_1 + Q_2 + Q_3. \qquad (33)$$

3.5 Parameters Used

We have taken a channel 2D domain for simulation, where the height of the channel is 100 and length of the channel is 1000 lattice units. Slip boundary conditions has been taken at the walls and velocity inlet and pressure outlet has been considered at the inlet and outlet respectively. The slip length taken here varying between 0 (for no-slip scenario) to 5 lattice units in corresponding simulations and theory predictions.

4   Results and Discussion

In our comprehensive investigation of fluid dynamics, we delved into the intricacies of two crucial boundary conditions: slip and no-slip. However, it is the slip condition that has captured our attention most prominently. This condition has unveiled a striking phenomenon in the velocity profile of a Newtonian fluid. Unlike the conventional no-slip scenario, where the fluid particles adhere rigidly to the solid boundary and exhibit zero velocity at the wall, the slip condition has unveiled a different story.

Under the slip condition, we observed a remarkable increase in velocity near the solid walls. This noteworthy departure from the no-slip scenario suggests the presence of a fundamental phenomenon known as 'boundary slip.' In simple terms, boundary slip implies that the fluid molecules in immediate contact with the solid boundary experience enhanced mobility and do not adhere as firmly as they do in the no-slip condition. The implications of this boundary slip are far-reaching and can be of paramount importance in various practical applications. It has the potential to influence heat transfer, mass transport, and overall fluid behavior in systems with small dimensions, such as microfluidic channels or nanoscale conduits. By allowing fluid molecules to move more freely near the boundary, slip conditions can alter the shear stress distribution and fundamentally affect the dynamics of fluid flow.

To order to show the contrast between slip and no-slip boundary conditions flow characteristics, we plot the velocity profile and strain rate profile in figure 3. This visual representation serves as a

powerful testament to the profound impact of boundary slip on fluid behavior, highlighting the need for careful consideration of this phenomenon in fluid dynamics research and engineering applications. In
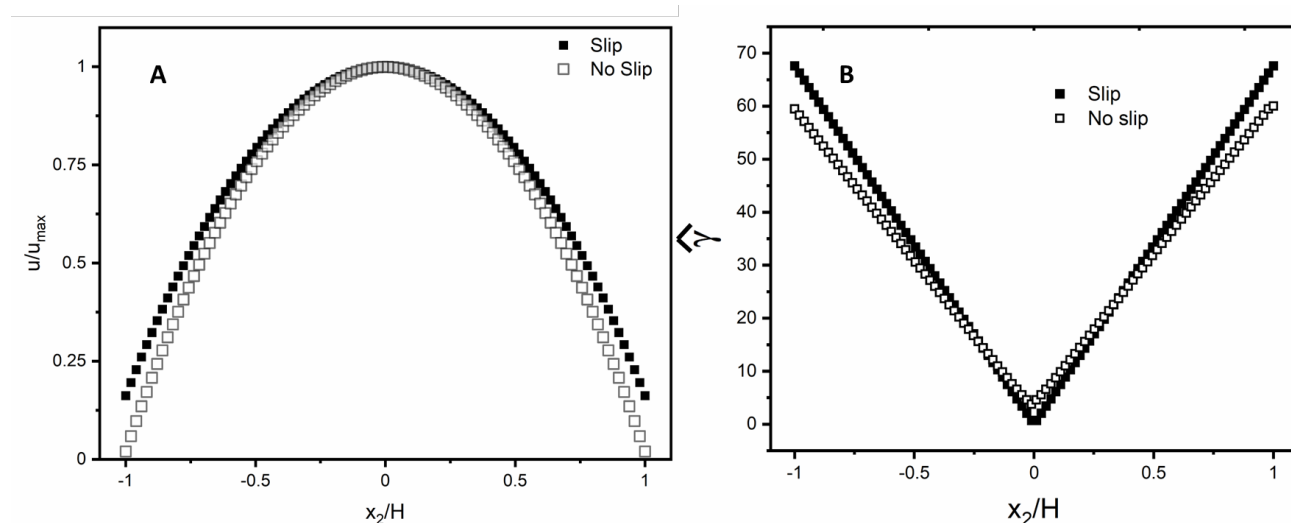

Figure 3: Slip and no slip boundary condition comparison of Newtonian fluid (A) Velocity profile (B) Strain rate profile.

our research, we extended our analysis to explore the behavior of a shear-thinning fluid with a power law index of 0.8. This distinctive fluid property introduces a new dimension to our understanding of fluid dynamics compared to the Newtonian counterpart. One of the most striking observations in the case of a shear-thinning fluid with a power law index of 0.8 is the unique velocity profile near the boundary walls. Unlike the behavior in a Newtonian fluid, where the velocity distribution primarily depends on the viscosity, in a shear-thinning fluid, the power law index comes into play. A power law index of 0.8 indicates that the fluid exhibits a decreasing viscosity with an increasing shear rate.

As a result, we found that near the solid walls, where the shear rates are typically higher due to the no-slip condition, the velocity of the shear-thinning fluid is significantly enhanced compared to a Newtonian fluid. This enhanced velocity near the walls can be attributed to the lower effective viscosity of the shear-thinning fluid in high-shear regions. This discovery carries substantial implications, particularly for applications involving non-Newtonian fluids. The power law index of 0.8 introduces a unique sensitivity to shear rate, making it a valuable parameter to consider in designing systems involving such fluids. Understanding how the power law index influences velocity profiles and strain rates is essential for optimizing processes in various industries, including pharmaceuticals, food processing, and oil extraction. Figure 4 illustrates the velocity profile and strain rate vs viscosity profile for the shear-thinning fluid with a power law index of 0.8. This shows the impact of non-Newtonian behavior on fluid dynamics and underscores the importance of considering rheological properties when working with shear-thinning fluids.

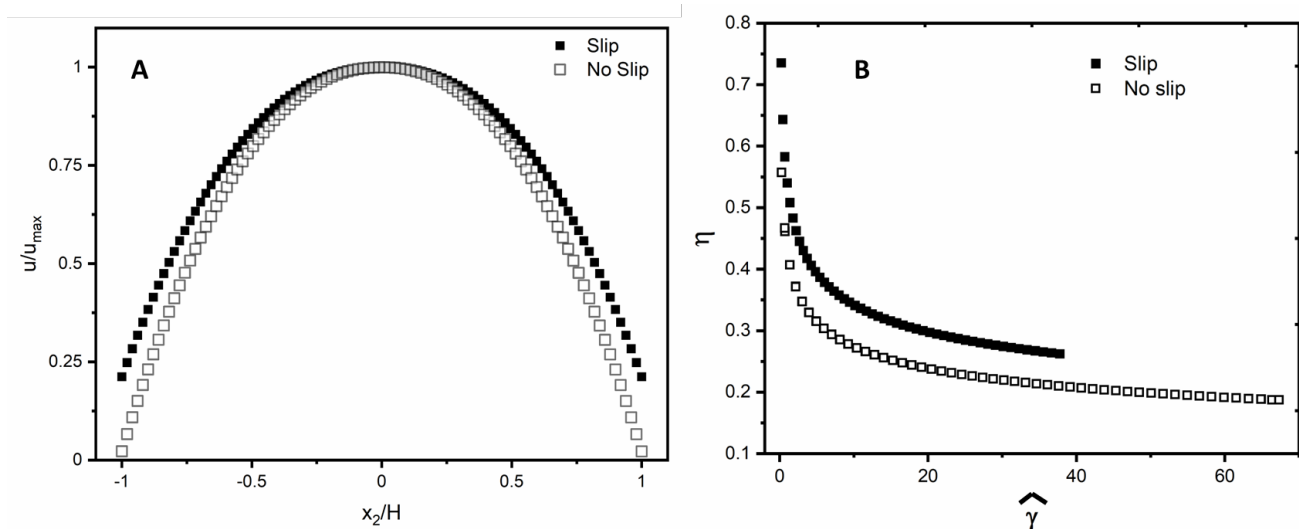Now, let's turn our attention to the shear-thickening fluid with a power law index of 1.4. This fluid

Figure 4: Slip and no slip boundary condition comparison of non-Newtonian fluid (n=0.8,m=0.05) (A) Velocity profile (B) Strain rate vs viscosity profile.
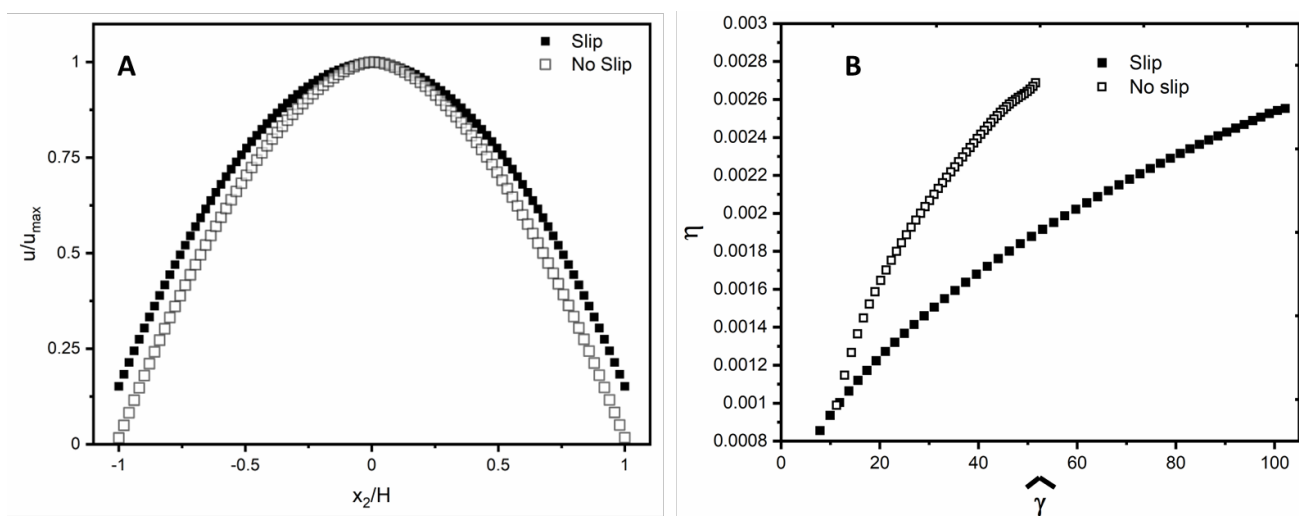

Figure 5: Slip and no slip boundary condition comparison of non-Newtonian fluid (n=1.4, m=0.05) (A) Velocity profile (B) Strain rate vs viscosity profile.

behaves differently from shear-thinning fluids; it exhibits increasing viscosity with increasing shear rate. In our analysis, we observed that this shear-thickening fluid displayed a notable reduction in velocity near the solid walls compared to the fluid with a power law index of 0.8 and a Newtonian fluid. The increase in viscosity near the wall due to the higher power law index led to a suppression of fluid motion close to the boundary. In figure 5, we have shown the velocity profiles and strain rate vs. viscosity profiles for both the shear-thinning fluid with a power law index of 0.8 and the shear-thickening fluid

with a power law index of 1.4. Figure Both figures 4 and 5 show the divergent effects of non-Newtonian behavior. It underscores how distinct power law indices can result in disparate velocity distributions and underscores the critical importance of meticulously accounting for rheological properties in systems involving these complex fluids.

A real shear-thickening fluid exhibits a unique combination of Newtonian, shear-thinning, and shear-thickening behaviors [3]. To comprehend the attributes of such a fluid, we have analyzed the viscosity variation with shear rate, as illustrated in Figure 6. The experimental variation of the real shear-thickening fluid is represented by black circles, while the model fit, determined using equation (13), is depicted by the red line. Our fit yielded power-law indices for the shear-thinning and shear-thickening regions (regions 2 and 3) as $n_1 = 0.8$ and $n_2 = 1.8$, respectively. Additionally, we calculated the corresponding consistency index coefficients as $m_1 = 0.065$, $m_2 = 0.0099$, and $m_3 = 34.30$.
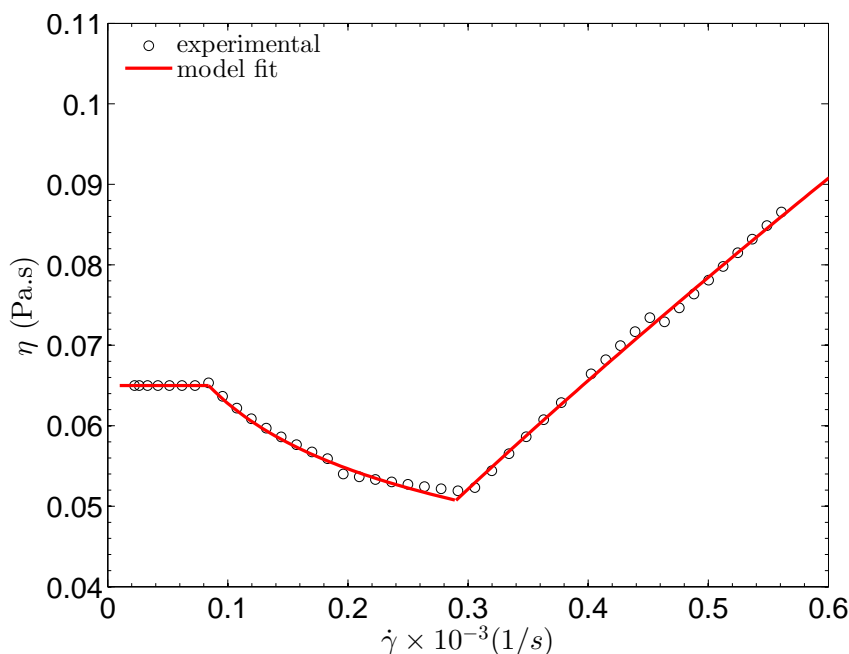

Figure 6: The correlation between strain rate and viscosity in a real shear-thickening fluid is depicted in the plot. The experimental parameters of the real shear-thickening fluid are represented by black circles, while the model fit, derived using equation (13), is illustrated by the red line. The analysis reveals three distinct regimes: starting from Newtonian behavior at initial shear rates, transitioning to shear-thinning behavior at moderate shear rates, and finally entering the thickening regime at higher applied shear rates.

In Figure 7, we have plotted the velocity profile calculated using the LBM and the theoretical model derived in section 4 for the three-phase real STF viscosity model. The blue, magenta and green symbols show the flow characteristics calculated using LBM at (a) $\lambda = 0$ lu, (b) $\lambda = 1$ lu, and (c) $\lambda = 5$ lu, respectively, and the multicolor dashed line shows the predictions using the derived model with regimes
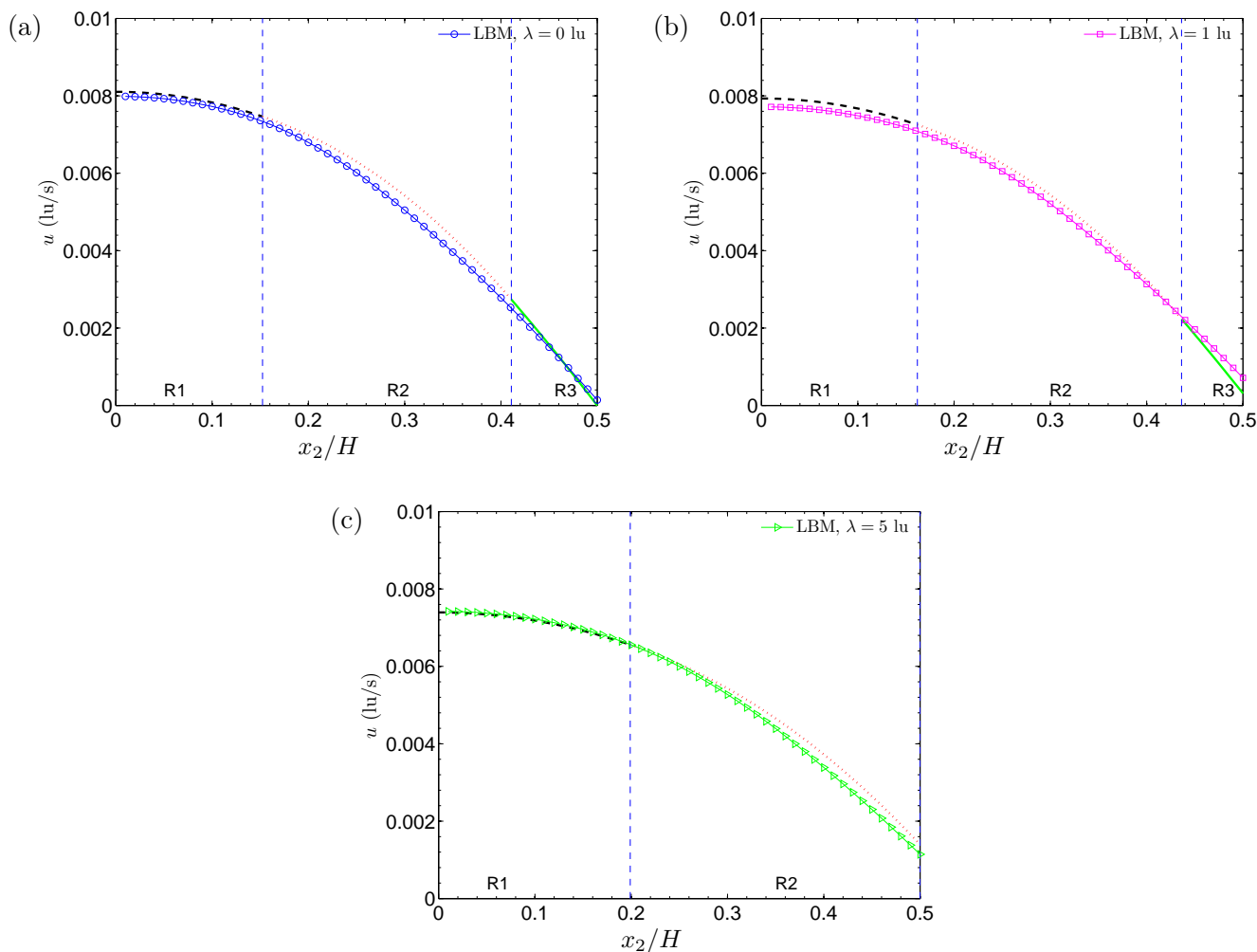
13

Figure 7: The flow characteristics of a real shear thickening fluid at various slip length of (a) $\lambda = 0$ lu, (b) $\lambda = 1$ lu, and (c) $\lambda = 5$ lu, respectively.

R1, R2, and R3, respectively. As shown, we find a good agreement between the two. The fluid is found to segregate with Newtonian flow at low shear rates at the centreline of the channel, transitioning to shear-thinning dominance in the intermediate region between the core and the channel-walls, and finally observing shear thickening phenomena as shear rates increase near the wall as shown with R1, R2 and R3, respectively. The appearance of the behavior occurs due to the high strain rates at the walls of the channels and low at the center of the channel. We show the comparison of magnitude of velocities as a effect of the slip-length for the same flow rate Q in figure 8. We find that the magnitude of the flow velocity near the centerline decreases and also near the wall increases as we increase the slip length. This phenomenon is found in both the LBM studies and the predictions from the theoretical model.

After validation of the LBM predictions with the analytical theoretical model prediction, we now discuss about the Effect of varying pressure on flow characteristics of real STF viscosity fluid when
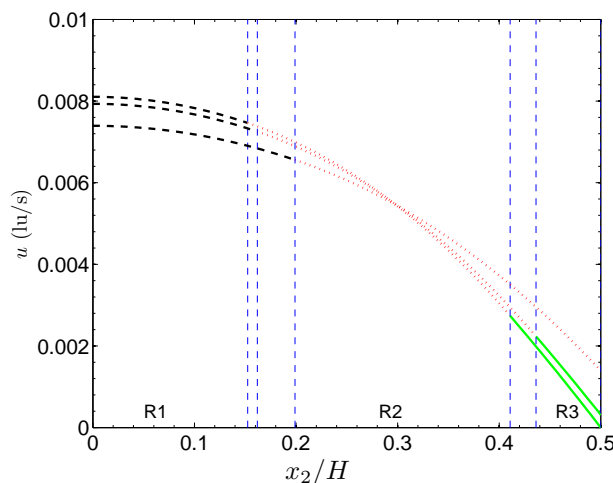
14

Figure 8: The comparison of magnitude of velocities as a effect of the slip-length for the same flow rate

wall-slip is present in the following sections.

4.1   Effect of varying pressure on flow characteristics of real STF viscosity fluid
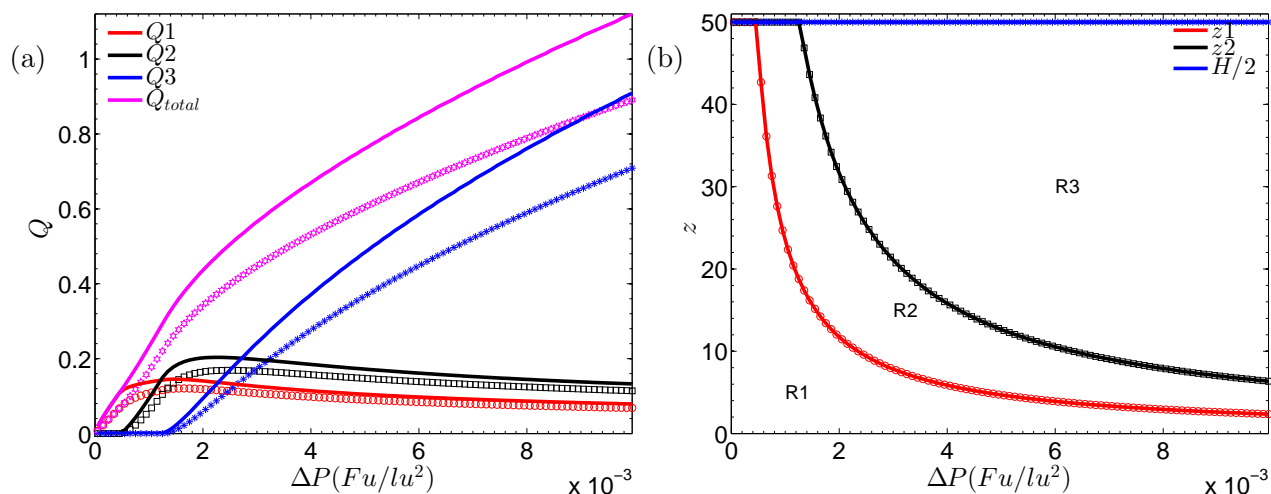

Figure 9: We show for the given real mimicked STF viscosity in (a) how flow rate in the upper half of the channel per unit width varies as a function of pressure and in (b) the region height varies as a function of pressure. Here, $Q1, Q2,$ and $Q3$ are the flow rates in regions 1 (Newtonian core), 2 (shear thinning intermediate), and 3 (shear thickening near channel wall), respectively. The symbols and the solid lines of the same color show the flow rates and the region height for slip length $\lambda = 0$ lu (as shown by Vishal et al. [20]) and 5 lu, respectively.

In Figure 9, we show for the given real mimicked STF viscosity, in (a) how flow rate per unit width varies as a function of pressure and in (b) the region height varies as a function of pressure. The

15

symbols and the solid lines of the same color show the flow rates and the region height for slip length $\lambda = 0$ lu (as shown by Vishal et al. [20]) and 5 lu, respectively. Here, $Q1, Q2,$ and $Q3$ are the flow rates in regions 1 (Newtonian core), 2 (shear thinning intermediate), and 3 (shear thickening near channel wall), respectively. We find that at very low pressure drop, the flow in the channel fully starts with Newtonian flow, as shown with red circles (as we can see the $z = H/2$ for the region R1); as we further increase pressure, the region R2 starts to appear (shown with black squares), and now Newtonian and thinning flow together (Newtonian in core and thiining in outer region) exist approximately for pressure $p < 2Fu/lu^2$ for both slip-lengths. Further, as we keep increasing the pressure drop, the shear rate's magnitude increases, and the channel's thickening flow dominates (shown with a blue asterisk line). We find at a low shear rate, $Q1$ dominates, reaching a maximum value up to where the increasing pressure for over constant or decreasing regional height $z1$ dominates the increment of flow; further, after that, the decreasing height $z1$ dominates over increasing pressure, and the net flow magnitude of $Q1$ decreases due to decrement of the $z1$. The same appears for $Q2$. On the other hand, the flow remains zero for Q3 up to a certain pressure until the shear rate becomes more than 0.3×10^{-3} 1/s; after that, the $Q3$ monotonically increases. We further find that, as the slip-length λ increases, the magnitude of the flow also increases for the same pressure drop.
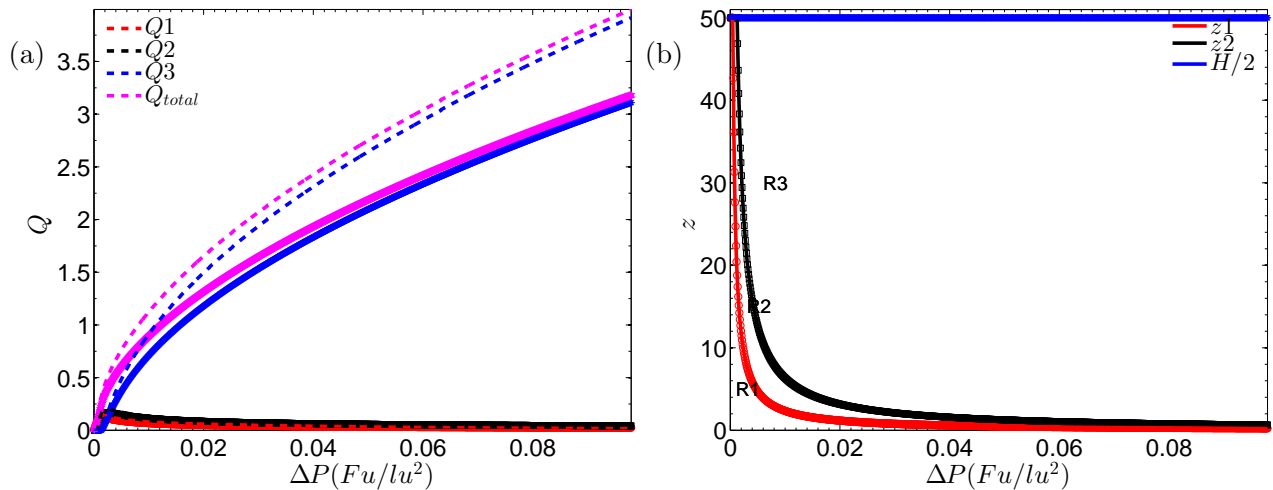

Figure 10: We show for the given real mimicked STF viscosity in (a) how flow rate in the upper half of the channel per unit width varies as a function of pressure and in (b) the region height varies as a function of pressure. Here, $Q1$, $Q2$, and $Q3$ are the flow rates in regions 1 (Newtonian core), 2 (shear thinning intermediate), and 3 (shear thickening near channel wall), respectively. The symbols and the dashed lines of the same color show the flow rates and the region height for slip length $\lambda = 0$ lu (as shown by Vishal et al. [20]) and 5 lu, respectively.

We also find that initial at low pressure the flow rate varies linearly when Newtonian flow dominates, i.e. (equation) , followed by increment in the flow rate-pressure slope from linear to $1/(m + 1)$, i.e. (equation). Further increment of pressure decreases the slope from $1/(m + 1)$ to 1 where the viscosity

16

increases from lowest thinning value to the Newtonian value, and at large pressure the flow rate-pressure slope reaches a constant value where it is proportional to (equation). This is true for both the slip-lengths. Further as the region height $z1$ and $z2$, do not explicitly depends on the slip-length, hence for both without slip and with slips, for the given pressure drop and other viscosity parameters, the region height remains same as we find in figure 9(b) for both $\lambda = 0$ lu (symbols, as shown by Vishal et al. [20]), and $\lambda = 5$ lu (solid lines), respectively.

In figure 10, we show the flow characteristic at the much larger magnitude of the pressure drop. We find that as we increase the pressure drop to a large extent, the $Q1$ and $Q2$ approaches to zero, and
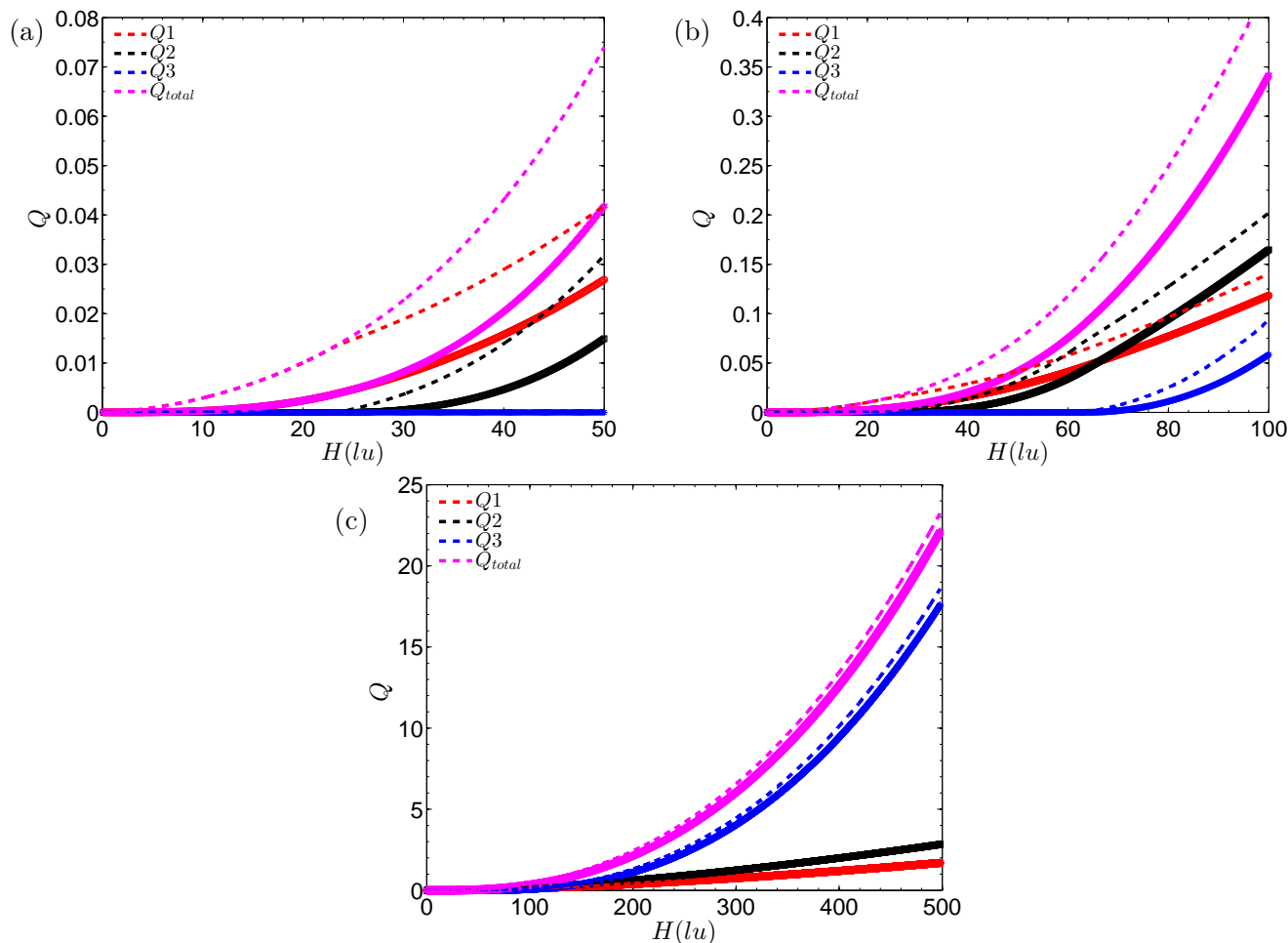

Figure 11: For the given real shear thickening fluid viscosity, we show (a) how the flow rate in the upper half of the channel per unit width varies as a function of the channel's height. Here, $Q1, Q2$, and $Q3$ are the flow rates in regions 1 (Newtonian core), 2 (shear thinning intermediate), and 3 (shear thickening near channel wall), respectively. The symbols and the dashed lines of the same color show the flow rates and the region height for slip length $\lambda = 0$ lu (as shown by Vishal et al. [20]) and 5 lu, respectively.

17

the channel flow with the thickening characteristics of the flow due to more significant shear rates in the channel. These phenomenon are true for both the $\lambda = 0$ lu (symbols), and $\lambda = 5$ lu (solid lines), respectively.

4.2 Effect of varying channel's height on flow characteristics of real STF

Finally, we study the effect of the channel's height on the flow characteristics of real STF flow. In Figure 11, we show for the given real mimicked STF viscosity, in (a) how flow rate varies as a function of the channel's height. The symbols and the dashed lines of the same color show the flow rates and the region height for slip length $\lambda = 0$ lu and 5 lu, respectively. Here, $Q1, Q2$, and $Q3$ are the flow rates in regions 1 (Newtonian core), 2 (shear thinning intermediate), and 3 (shear thickening near channel wall), respectively.

Further, we study the effect of varying channel's height on flow characteristics of real STF viscosity fluid with slip-effects and compare it without slip flow characteristics as shown by Vishal et al. [20]. In Figures 11(a), (b), and (c), we plotted the flow rate up to 50, 100, and 500 lattice units. The symbols and the dashed lines of the same color show the flow rates and the region height for slip length $\lambda = 0$ lu and 5 lu, respectively. From these three figures, we find that for low heights, $Q1$ dominates for given viscosity, and as H increases to a larger order, $Q2$ and $Q3$ start to dominate. This is because, for a given pressure difference, the stress (and hence the corresponding shear rate) is linearly proportional to the height of the channel. As the shear rate increases, the viscosity of the fluid shifts from Newtonian to thinning behavior and then to thickening behaviors, which initially makes $Q1$ dominate, followed by $Q2$ and $Q3$, respectively. These phenomenon are true for both the $\lambda = 0$ lu (symbols), and $\lambda = 5$ lu (solid lines), respectively. Although the magnitude rise of the flow rate with slips are more in comparison to the flow rate without slips.

5 Conclusion

In the present investigation, we have highlighted the impact of slip boundary condition in a channel on the rheological properties, power law indices, and on fluid velocity profiles. We examined the impact of a real shear-thickening fluid on the velocity profile and pressure drop within the specified domain. Initially, we conducted analytical calculations for the channel flow, considering three distinct regions with Newtonian, shear-thinning, and shear-thickening properties of the real shear-thickening fluid. A comparative analysis of the flow characteristics obtained through lattice Boltzmann methods was then carried out against the predictions of the theoretical model. Additionally, we explored the shear rate-dependent viscosity of the fluid as it flows through the channel, employing the lattice Boltzmann method. Firstly, our exploration of shear-thinning and shear-thickening fluids with power law indices of 0.8 and 1.4, respectively, revealed contrasting behaviors. A power law index of 0.8 led to enhanced velocities near the solid walls due to decreasing viscosity with increasing shear rate, while a power law index of 1.4, characteristic of shear-thickening fluids, caused a reduction in wall velocities as viscosity increased

with shear rate. Furthermore, our study extended to real shear-thickening fluids, combining all the Newtonian, the shear-thinning and the shear-thickening effects. Incorporating strain rate vs. viscosity data, we observed intricate variations in velocity profiles. Particularly noteworthy was the discovery that employing slip boundary conditions resulted in significantly higher wall velocities, underlining the importance of boundary conditions in complex fluid systems.

We extend our investigation to explore the impact of varying pressure and channel height on the flow characteristics of real shear-thickening fluid viscosity. Our findings reveal a nuanced response to increasing pressure: initially, the flow rate $Q1$ takes precedence, reaching a maximum value. Subsequently, as pressure continues to increase over constant/decreasing regional height $z1$, $Q1$ starts to decline due to the decrement in $z1$, and $Q2$ becomes dominant, with flow remaining zero for $Q3$. Upon further escalating the threshold pressure until the shear rate surpasses a certain threshold, $Q3$ exhibits a monotonically increasing trend, ultimately becoming dominant. At this juncture, both $Q1$ and $Q2$ approach asymptotically to zero. These phenomena hold true for both scenarios, with and without slip effects. Notably, flow rate magnitudes are higher with slips for a given pressure drop and viscosity characteristics within a specified channel domain.

Further, when the channel's height increases, we observe that, at lower heights, the flow rate $Q1$ predominates for a given real shear-thickening fluid viscosity profile. As the channel height (H) increases to a larger extent, $Q2$ and subsequently $Q3$ begin to dominate. This trend is attributed to the linear proportionality between stress (and thus shear rate) and the channel's height for a given pressure difference. With increasing shear rates, the fluid's viscosity undergoes a transition from Newtonian to shear-thinning and then shear-thickening behaviors, causing a sequential dominance of $Q1$, followed by $Q2$ and $Q3$. These observations hold true for both scenarios, with and without slip effects. It is noteworthy that flow rate magnitudes are higher with slips for a given pressure drop and viscosity characteristics within a specified channel domain.

References

[1] Abdelhalim Ebaid, Fahd Al Mutairi, SM Khaled, et al. Effect of velocity slip boundary condition on the flow and heat transfer of cu-water and tio 2-water nanofluids in the presence of a magnetic field. *Advances in Mathematical Physics*, 2014, 2014.

[2] Phil Ligrani, Danny Blanchard, and Bruce Gale. Slip due to surface roughness for a newtonian liquid in a viscous microscale disk pump. *Physics of Fluids*, 22(5), 2010.

[3] Kai Wang, Zhenhua Chai, Guoxiang Hou, Wei Chen, and Sheng Xu. Slip boundary condition for lattice boltzmann modeling of liquid flows. *Computers & Fluids*, 161:60–73, 2018.

[4] Zhaoli Guo, Baochang Shi, TS Zhao, and Chuguang Zheng. Discrete effects on boundary conditions for the lattice boltzmann equation in simulating microscale gas flows. *Physical Review E*, 76(5): 056704, 2007.

[5] IJ Rao and KR Rajagopal. The effect of the slip boundary condition on the flow of fluids in a channel. *Acta Mechanica*, 135(3-4):113–126, 1999.

[6] Ashish Garg. Enhanced flow in deformable carbon nanotubes. *Journal of Applied Physics*, 135(7), 2024.

[7] Ashish Garg and Swati Bishnoi. An empirical experimental observations and md simulation data-based model for the material properties of confined fluids in nano/angstrom size tubes. *Nano Express*, 2023. doi: 10.1088/2632-959X/ad2b83.

[8] Taha Sochi. Slip at fluid-solid interface. *Polymer Reviews*, 51(4):309–340, 2011.

[9] A Vikhansky. Lattice-boltzmann method for yield-stress liquids. *Journal of Non-Newtonian Fluid Mechanics*, 155(3):95–100, 2008.

[10] Chen-Hao Wang and Jeng-Rong Ho. A lattice boltzmann approach for the non-newtonian effect in the blood flow. *Computers & Mathematics with Applications*, 62(1):75–86, 2011.

[11] Xiaoyi He and Li-Shi Luo. Theory of the lattice boltzmann method: From the boltzmann equation to the lattice boltzmann equation. *Physical review E*, 56(6):6811, 1997.

[12] Edo S Boek and Maddalena Venturoli. Lattice-boltzmann studies of fluid flow in porous media with realistic rock geometries. *Computers & Mathematics with Applications*, 59(7):2305–2314, 2010.

[13] Zhi-Wei Tian, Chun Zou, Hong-Juan Liu, Zhao-Li Guo, Zhao-Hui Liu, and Chu-Guang Zheng. Lattice boltzmann scheme for simulating thermal micro-flow. *Physica A: Statistical Mechanics and its Applications*, 385(1):59–68, 2007.

[14] Lin Zheng, Bao-Chang Shi, and Zhen-Hua Chai. Lattice boltzmann method for simulating the temperature jump and velocity slip in microchannels. *Communications in computational physics*, 2 (6):1125–1138, 2007.

[15] Ashish Garg. Fluidisation of yield stress materials under vibration. *PhD thesis, The University of Manchester*, pages 1–175, 2022.

[16] Georges Bossis, Olga Volkova, Yan Grasselli, and Oumar Gueye. Discontinuous shear thickening in concentrated suspensions. *Philosophical Transactions of the Royal Society A*, 377(2143):20180211, 2019.

[17] GG Pereira. Effect of variable slip boundary conditions on flows of pressure driven non-newtonian fluids. *Journal of non-newtonian fluid mechanics*, 157(3):197–206, 2009.

[18] Ren Jie Chin, Sai Hin Lai, Shaliza Ibrahim, and Wan Zurina Wan Jaafar. Factors affect wall slip: particle size, concentration, and temperature. *Applied Rheology*, 28(1):201815775, 2018.

[19] Patrick Wilms, Jan Wieringa, Theo Blijdenstein, Kees van Malssen, and Reinhard Kohlus. Quantification of shear viscosity and wall slip velocity of highly concentrated suspensions with non-newtonian matrices in pressure driven flows. *Rheologica Acta*, 60(8):423–437, 2021.

[20] Garima Vishal, Ashish Garg, Jayati Sarkar, and Sudip K Pattanayek. The channel flow of a real shear thickening fluid using the lattice boltzmann simulation and the theoretical model. *ChemRxiv-Chemical Engineering and Industrial Chemistry, DOI: 10.26434/chemrxiv-2023-zk1nn*, pages 1–26, 2023.

[21] Garima Vishal, Ashish Garg, Jayati Sarkar, and Sudip Kumar Pattanayek. Real shear thickening fluid (stf) flow in converging-diverging channels: Analytical and lattice boltzmann study. *ChemRxiv-Chemical Engineering and Industrial Chemistry, DOI: 10.26434/chemrxiv-2023-3cjvq*, pages 1–29, 2023.

[22] Ashish Garg. Pulsatile pressure enhanced rapid water transport through flexible graphene nano/angstrom-size channels: a continuum modeling approach using the micro-structure of nanoconfined water. *New Journal of Physics*, 25(10), 2023.

[23] Ashish Garg. Aerodynamics. In *GATE Aerospace Forum Educational Services*, 2015.

[24] James P Kelliher. Navier–stokes equations with navier boundary conditions for a bounded domain in the plane. *SIAM journal on mathematical analysis*, 38(1):210–232, 2006.

[25] Ivan C Christov, Vincent Cognet, Tanmay C Shidhore, and Howard A Stone. Flow rate–pressure drop relation for deformable shallow microfluidic channels. *Journal of Fluid Mechanics*, 841:267–286, 2018.

[26] Ashish Garg and Pranjal Prasad. Yield–stress shear thinning and shear thickening fluid flows in deformable channels. *Physica Scripta*, 99(3), 2023. doi: 10.1088/1402-4896/ad2898.

[27] Raj P Chhabra and John Francis Richardson. *Non-Newtonian flow and applied rheology: engineering applications.* Butterworth-Heinemann, 2011.